# A Robust Wireless Power Transfer System With Self-Alignment Capability and Controllable Output Current for Automatic-Guided Vehicles

Xiaofei Li, *Member, IEEE*, Cheng Wang, Heshou Wang, Xin Dai, *Member, IEEE*, Yue Sun, *Member, IEEE*, and Aiguo Patrick Hu, *Senior Member, IEEE*

***Abstract*—In this article, a robust wireless power transfer system is proposed with self-alignment capability and controllable output current characteristics for static charging of automatic-guided vehicles (AGVs). A reconfigurable circuitry is designed to work initially in an inductor–capacitor–capacitor-series compensation mode for achieving magnetic field self-alignment, then switched to the *LCC–LCC* configuration for wireless charging. Apart from the passive components used for wireless power transfer, no additional components, such as cameras, sensors, or dedicated sensing coils, are needed for self-alignment. The induced voltage of a series-tuned Q-coil on the load side is used for the AGV to automatically adjust its position. The vehicle will be self-aligned when the induced voltage becomes null, then the system is switched to a controllable constant current charging mode. A prototype is built, which demonstrates that the output charging current is controllable and can be kept constant against load variations. The experimental results show the proposed system can realize an 89.1% dc–dc power transfer efficiency at an output current of 30 A and an output voltage of 48 V.**

***Index Terms*—Automatic-guided vehicles (AGVS), output control, self-alignment, wireless power transfer (WPT).**

## I. Introduction

INDUSTRY 4.0 reveals that a tremendous transformation is taking place in industrial automation in the direction of intelligent manufacturing. Both industry and academia have expressed concern about intelligent manufacturing since it has the potential to enable customized production, reduce energy consumption, and lower labor costs [1]. Among different unmanned devices, automatic-guided vehicles (AGVs) play an important role in cargo handling and allocation in the unmanned manufacturing industry because of their outstanding advantages. For example, strong adaptability, high work efficiency, easy navigation settings, high intelligence, and convenient scheduling all make the AGV become an ideal choice for unmanned logistics management systems [2]. When equipped with a guidance device and motor control system, AGVs can follow a guided route without any human involvement. Therefore, AGVs are urgently needed in industrial facilities in order to improve transportation efficiency and save labor costs.

To further realize automation, the conventional conductive charging system seems not a wise choice. As an intelligent alternative, wireless power transfer (WPT) is more suitable for AGVs [3]. Compared with traditionally conductive charging systems, wireless chargers serve as a concise and practical power supply. Nowadays, it has gained attention globally and has been successfully equipped with numerous industrial applications, such as household appliances and mobile phones.

Unlike static wireless charging for smartphones, wireless charging for AGVs should take misalignment into consideration. For example, Fig. 1 illustrates one typical static wireless charging system for AGVs. It was commonly recognized that the AGV charging performance highly relies on the positions between transmitting coils and receiving coils. In other words, misalignment greatly deteriorates the resonant state and power transfer efficiency (PTE). Thus, it is necessary to investigate the alignment approaches to realize a user-friendly and robust wireless charging system for vehicles.

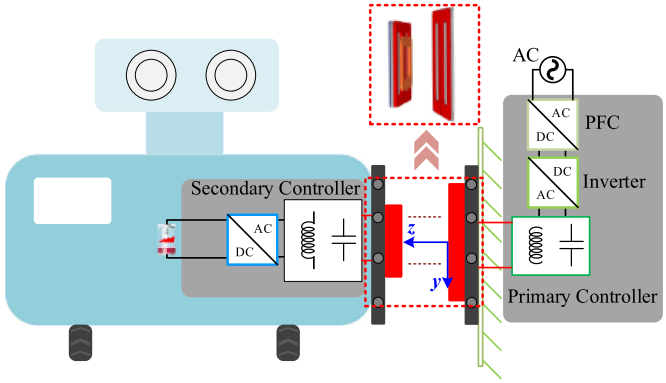


Fig. 1. Front view of a typical static WPT system for AGVs.

Manuscript received 17 February 2023; revised 12 June 2023; accepted 16 July 2023. Date of publication 20 July 2023; date of current version 1 September 2023. This work was supported by the National Natural Science Foundation of China under Grant 52007012. *(Corresponding authors: Xiaofei Li; Cheng Wang.)*

Xiaofei Li, Cheng Wang, Xin Dai, and Yue Sun are with the School of Automation, Chongqing University, Chongqing 400016, China (e-mail: xiaofei.li@cqu.edu.cn; whih5776@163.com; toybear@vip.sina.com; syue06@cqu.edu.cn).

Heshou Wang is with the Department of Electrical Engineering, The Hong Kong Polytechnic University, Hong Kong (e-mail: crane89757@gmail.com).

Aiguo Patrick Hu is with the Department of Electrical and Computer Engineering, University of Auckland, Auckland 1142, New Zealand (e-mail: a.hu@auckland.ac.nz).

Color versions of one or more figures in this article are available at https://doi.org/10.1109/TPEL.2023.3297196.

Digital Object Identifier 10.1109/TPEL.2023.3297196

One classical alignment method for WPT systems is to adopt cameras [4], ultrasonic sensors [5], or radio frequency identification (RFID) sensors [6]. However, these additional devices are not only expensive but also easily affected by rough weather conditions. To avoid using costly auxiliary equipment, a mutual inductance detection method is proposed to assist the position correction in [7], while a primary current (or secondary current) detection method is proposed to assist the alignment in [8] or [9]. Nevertheless, the mutual inductance detection is technically complicated since many electric parameters are required to be detected. For example, Kobayashi et al. [10] calculate mutual inductance by detecting the voltage and current at the receiver side; and Dai et al. [11] calculate mutual inductance by detecting the voltage and the control variables at the receiver side. As for the primary or secondary current detection method, measuring the root-mean-square (RMS) value of the alternating currents is difficult. Therefore, recent research increasingly focuses on sensing coils due to their simplicity and robustness [12], [13]. However, these sensing coils are still auxiliary parts that may cause a bulky and redundant system. To resolve the aforementioned technical gap, in this article, we introduce a simple and practical WPT system with the function of self-alignment and controllable output current. The contributions and advantages of this article can be summarized as follows.

1) This article proposes a simple and practical self-alignment method for the WPT system. Compared to [4], [5], [6], [12], and [13], there is no need for additional components, such as cameras, sensors, or dedicated sensing coils. All the components contribute to the self-alignment and WPT. Moreover, the self-alignment ensures good magnetic coupling before charging, leading to a high mutual inductance and high PTE.
2) Well-designed magnetic coupling structure: The presented magnetic coupling structure eliminates the cross coupling between compensating coils and transmitting/receiving coils with the help of the decoupling phenomenon among the overlapped DD-coil and the Q-coil [14]. The Q-coil on the receiving side is used not only as the sensing coil in the self-alignment mode but also as the compensating inductor in the *LCC* topology in the charging state. And the sampling information for the alignment is the output dc voltage, which is more straightforward and easier to implement compared to [7], [8], and [9].
3) Interference rejection: The closed-loop control in this article not only realizes the handshake process in the self-alignment mode but also realizes interference rejection in the $y$-direction. Taking advantage of DD coils in the vertical direction, the corresponding misalignment, i.e., $y$-direction tolerance, is also improved, as shown in Fig. 1. This is extremely practical for industrial applications, such as AGVs and cargo-carrying robots. In the daily production process, the height of the chassis usually varies along with the total weight of the cargo. Hence, the $y$-direction misalignment must be considered for a reliable working environment in case of unexpected disturbances, such as mutual inductance changes.

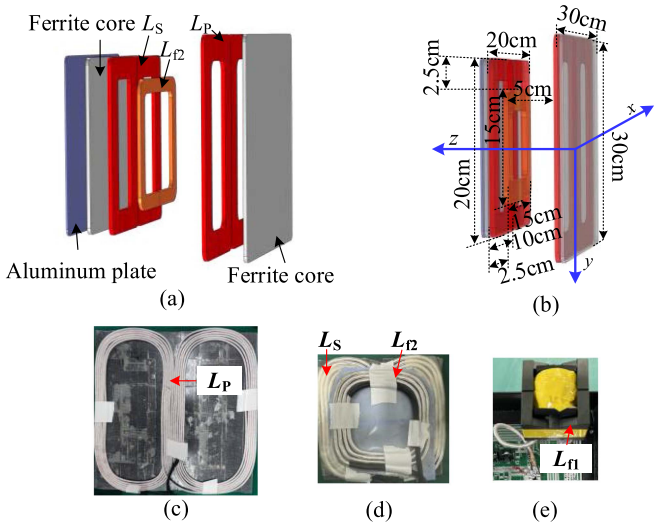


Fig. 2. Proposed magnetic coupling structure. (a) Overview. (b) Specific size information. (c) Picture of $L_P$. (d) Picture of $L_S$ and $L_{f2}$. (e) Picture of $L_{f1}$.

## II. Magnetic Coupling Mechanism

### A. Coupling Structure

Fig. 2(a) illustrates the presented magnetic coupling structure. The transmitting coil ($L_P$) and receiving coil ($L_S$) are both DD coils. The secondary-side compensation coil $L_{f2}$ is a Q-coil, which is placed in overlap with $L_S$, as shown in Fig. 2(b). The primary-side compensation coil $L_{f1}$ is wound on the E–E magnetic core. Ferrite cores are used on both sides to enhance the magnetic coupling from the transmitting to receiving side. An aluminum plate is adopted on the vehicle side to reduce the leakage electromagnetic field. The coupling structure of the primary and secondary sides is shown in Fig. 2(b) with the specific size information.

In this article, 600-strand Litz wire with a diameter of 3.4 mm is used to make the transmitting coil ($L_P$), while 6.5 mm 2000-strand Litz wire is adopted to make receiving coil ($L_S$) and compensating inductors ($L_{f2}$). The number of turns $N_p$, $N_{f2}$, and $N_S$ for $L_P$, $L_{f2}$, and $L_S$ will be detailed in Section IV, which are 6, 4, and 6, respectively. The thicknesses of the aluminum plate and the ferrite core are 2 mm and 4 mm, respectively. The pictures of $L_P$, $L_S$, $L_{f2}$, and $L_{f1}$ are shown in Fig. 2(c), (d), and (e), respectively.

### B. Mutual Inductance Variation

One advantage of the DD-coil is to improve the lateral misalignment tolerance in the door-to-door direction, i.e., the $y$-direction, as shown in Fig. 1 [15], which also benefits this article, as shown in Fig. 3(a). The variation of $M_1$ (i.e., the mutual inductance between $L_P$ and $L_S$) is from 6.6 to 8.0 $\mu$H within the specific misalignment region, i.e., $-8\text{ cm} \le y \le 8\text{ cm}$. The maximum mutual inductance difference is 1.4 $\mu$H over this region.

Fig. 3(b) illustrates the measured $M_2$ (i.e., the mutual inductance between $L_P$ and $L_{f2}$) within the specific misalignment area, i.e., $(-10\text{ cm}, 0\text{ cm}) \le (x, y) \le (10\text{ cm}, 8\text{ cm})$. It can

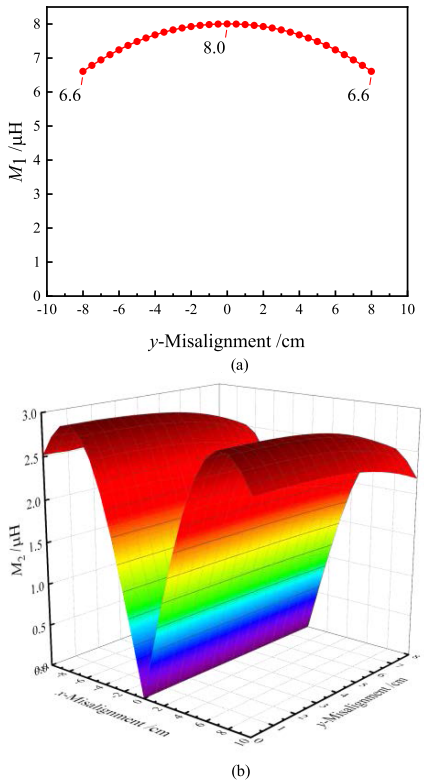


Fig. 3. Variation mutual inductance. (a) Mutual inductance $M_1$ between the transmitting DD-coil $L_P$ and the receiving DD-coil $L_S$ at different positions regarding the $y$-misalignment. (b) Variation of mutual inductance $M_2$ between the transmitting DD-coil $L_P$ and the receiving compensation Q-coil $L_{f2}$ at different positions regarding the $x$ and $y$ misalignments.

be seen that $M_2$ fluctuates with $x$, and this article utilizes such fluctuation for self-alignment. It shows that $M_2$ becomes 0 when $x$-misalignment is 0, which also means that the vehicle is well-aligned.

## III. Circuit Topology and System Control

### A. Circuit Topology

Fig. 4 demonstrates the circuit diagram of the proposed WPT system. With the help of the switch $S$, two compensating networks can be realized, i.e., the inductor–capacitor–capacitor-series (*LCC*-S) for self-alignment and the *LCC–LCC* compensation topology for normal charging operation. Switch $S$ is composed of two anti-series-connected MOSFETs (i.e., $S_1$ and $S_2$). For simplifying the analysis, the parasitic resistances of the coils are ignored.

$C_P$, $C_{f1}$, $C_{f2}$, and $C_S$ are the compensation capacitors, which satisfy the following equations:

$$\begin{cases} \omega^2 L_{f1} C_{f1} = 1 & \omega^2 (L_P - L_{f1}) C_P = 1 \\ \omega^2 L_{f2} C_{f2} = 1 & \omega^2 (L_S - L_{f2}) C_S = 1 \end{cases} \tag{1}$$

where $\omega$ is the operating angular frequency of power transfer, which satisfies $\omega = 2\pi f$. And $f$ is the operating frequency of the system.

Fig. 5 illustrates the equivalent circuit of the *LCC*-S compensation topology for self-alignment.

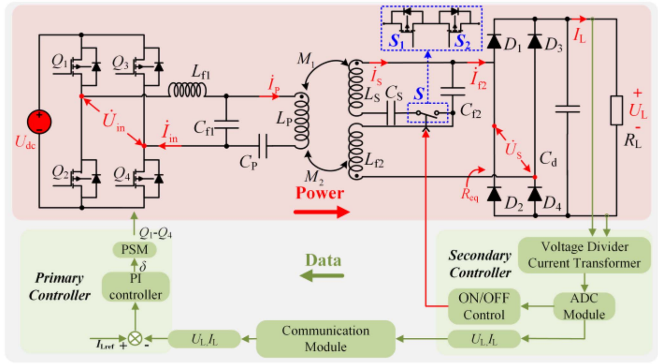


Fig. 4. Circuit diagram of the proposed WPT system.

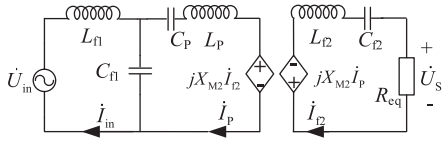

Fig. 5. Equivalent circuit with the *LCC*-S compensating topology.

In this article, phase-shifted modulation (PSM) is adopted to control the inverter, and the fundamental output voltage in phasor form can be written as follows [8]:

$$\dot{U}_{\text{in}} = \frac{2\sqrt{2}U_{\text{dc}}}{\pi} \sin\frac{\delta}{2} \angle 0^\circ \tag{2}$$

where $\delta$ is the conduction angle. By using Kirchhoff's voltage law (KVL), and according to the relationship between the input and output voltage of the rectifier [3], the following equations can be derived:

$$\begin{cases} \dot{U}_{\text{in}} = (jX_{Lf1} - jX_{Cf1})\,\dot{I}_{\text{in}} + jX_{Cf1}\dot{I}_p \\ 0 = (jX_{Lp} - jX_{Cp} - jX_{Cf1})\,\dot{I}_p + jX_{Cf1}\dot{I}_{\text{in}} - jX_{M2}\dot{I}_{f2} \\ 0 = -jX_{M2}\dot{I}_p + (jX_{Lf2} - jX_{Cf2} + R_{\text{eq}})\,\dot{I}_{f2} \\ \dot{U}_S = R_{\text{eq}}\dot{I}_{f2} \\ U_L = \frac{\pi\sqrt{2}}{4} U_S \end{cases} \tag{3}$$

where $U_S$ is the RMS value and

$$\begin{cases} X_{Lf1} = \omega L_{f1} & X_{Cf1} = 1/\omega C_{f1} \quad X_{Lp} = \omega L_P \\ X_{Cp} = 1/\omega C_P & \\ X_{Lf2} = \omega L_{Lf2} & X_{Cf2} = 1/\omega C_{Cf2} \quad X_{M2} = \omega M_2 \\ R_{\text{eq}} = 8R_L\left(\pi^2\right)^{-1}. & \end{cases} \tag{4}$$

Then, by substituting (1), (2), and (4) into (3), one can obtain

$$I_p = \frac{2\sqrt{2}}{\pi} \frac{U_{\text{dc}}}{\omega L_{f1}} \sin\frac{\delta}{2} \tag{5}$$

$$U_L = \frac{M_2 U_{\text{dc}}}{L_{f1}} \sin\frac{\delta}{2} \tag{6}$$

where $I_P$ is the RMS value of $\dot{I}_P$.

Fig. 6 shows the equivalent circuit with an *LCC–LCC* compensation topology. Here, the receiver side is well-aligned, and

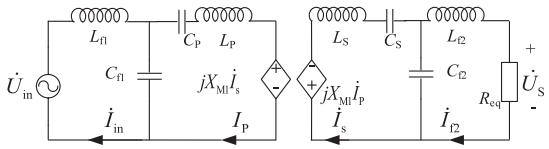


Fig. 6. Equivalent circuit with the *LCC–LCC* compensating topology.

the mutual inductance $M_2$ is eliminated because the Q-coil on the receiving side overlaps with the DD-coil on the transmitting side. Therefore, $M_2$ becomes 0 due to the decoupling phenomenon of Q-coil and DD-coil [8].

Similarly, the following equations can be derived by using KVL:

$$\begin{cases} \dot{U}_{\text{in}} = (jX_{Lf1} - jX_{Cf1})\,\dot{I}_{\text{in}} + jX_{Cf1}\dot{I}_p \\ 0 = (jX_{Lp} - jX_{Cp} - jX_{Cf1})\,\dot{I}_p + jX_{Cf1}\dot{I}_{\text{in}} - jX_{M1}\dot{I}_s \\ 0 = -jX_{M1}\dot{I}_p + (jX_{Ls} - jX_{Cs} - jX_{Cf2})\,\dot{I}_s + jX_{Cf2}\dot{I}_{f2} \\ 0 = (jX_{Lf2} - jX_{Cf2} + R_{\text{eq}})\,\dot{I}_{f2} + jX_{Cf2}\dot{I}_s \\ I_L = \frac{2\sqrt{2}}{\pi} I_{f2} \end{cases} \tag{7}$$

where $I_{f2}$ is the RMS value of $\dot{I}_{f2}$ and

$$X_{M1} = \omega M_1, \quad X_{Ls} = \omega L_S, \quad X_{Cs} = 1/\omega C_S. \tag{8}$$

Then, substituting (1), (2), and (8) into (7), (9), and (10) can be obtained, where $I_{\text{in}}$, $I_S$, and $I_{f2}$ are the RMS values of $\dot{I}_{\text{in}}$, $\dot{I}_S$, and $\dot{I}_{f2}$, respectively

$$\begin{cases} I_{\text{in}} = \dfrac{2\sqrt{2}}{\pi} \dfrac{M_1^2 U_{\text{dc}} R_{\text{eq}}}{\omega^2 L_{f1}^2 L_{f2}^2} \sin\dfrac{\delta}{2} \\ I_S = \dfrac{2\sqrt{2}}{\pi} \dfrac{M_1 U_{\text{dc}} R_{\text{eq}}}{\omega^2 L_{f1} L_{f2}^2} \sin\dfrac{\delta}{2} \end{cases} \tag{9}$$

$$I_L = \frac{8}{\pi^2} \frac{M_1 U_{\text{dc}}}{\omega L_{f1} L_{f2}} \sin\frac{\delta}{2} = \frac{2\sqrt{2}}{\pi} I_{f2}. \tag{10}$$

As can be seen from (10), it is obvious that the output current $I_L$ is irrelevant to the load, and the value of $I_L$ is determined by $\delta$, $U_{\text{dc}}$, $\omega$, $L_{f1}$, $L_{f2}$, and $M_1$.

### B. System Control

The control diagram of the proposed system is illustrated in Fig. 7. There are two controllers, i.e., the primary-side controller and the secondary-side controller. The conduction angle $\delta$ is first fixed as $\delta_0$ to initialize the entire system by transferring a small amount of energy to the receiver over a low-density magnetic field for self-alignment. To detect the position, the key information, i.e., the output voltage $U_L$, is sampled by the secondary-side controller. Using the A/D module after the voltage divider, this voltage information can be analyzed by the MCU STM32F334. The AGV would continue adjusting its position until $U_L$ is reduced to an error index $\alpha$ for the well-aligned condition ($\alpha$ tends to 0). In other words, the AGV arrives at the well-aligned position when the receiving Q-coil is decoupled from the transmitting DD-coil. Then, the receiving-side controller sends a handshaking signal to the transmitting side to start the constant current (CC) charging with a conduction angle $\delta_0$. The primary controller picks up the information of $I_L$ by using wireless

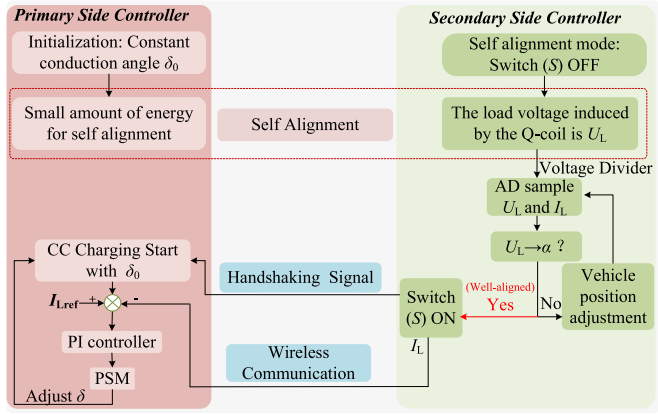


Fig. 7. Diagram showing the system control strategy.

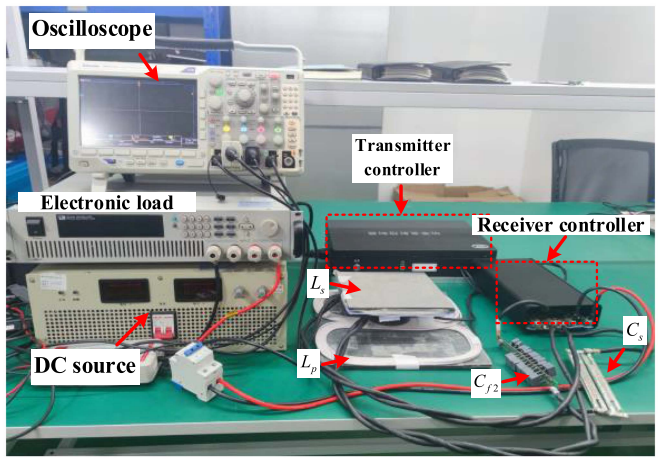


Fig. 8. Picture of the presented experimental setup.

communication. The error between the feedback voltage $I_L$ and the reference $I_{L\text{ref}}$ is sent to the proportional–integral controller, and then, the processed result is delivered to the PSM controller for conduction angle $\delta$ calculation to regulate the output current.

## IV. Experimental Validation

A laboratory prototype is built, as shown in Fig. 8. The utilized wireless communication module is G01-SPIPX Si24R1 from Ashining Technology. The MOSFET $S_1$ and $S_2$ used in this article are H1M065F020 from Hestia Power.

The design flowchart of the system parameters is shown in Fig. 9. Since the dc voltage source $U_{\text{dc}}$, the operating frequency $f$, the primary current $I_P$, the load $R_L$ and the desired $U_L$ and $I_L$ are given, $I_{f2}$ can be determined by (10), and then the wire sizes of $L_P$ and $L_{f2}$ can be selected accordingly. $L_{f1}$ can be determined by (5), and according to the desired output voltage $U_L$, $M_2$ can be further determined by (6). The turns $N_p$ and $N_{f2}$ are changed to realize the desired $M_2$. Then, according to the desired output current $I_L$, $M_1$ can be determined by (10). $I_{\text{in}}$ and $I_S$ can be determined by (9), and then the wire sizes of $L_{f1}$ and $L_S$ can be selected accordingly. The turns $N_S$ is changed to realize the desired $M_1$. Next, based on (1), the corresponding

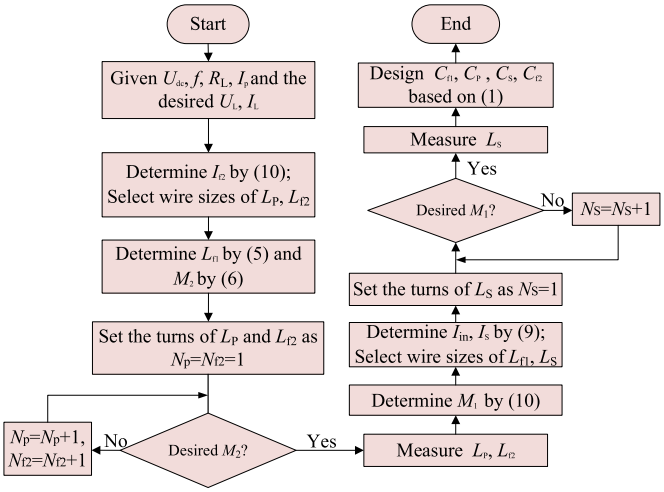


Fig. 9. Design flowchart of system parameters.

TABLE I
SYSTEM PARAMETERS

| $M_1$ | $L_P$ | $L_S$ | $L_{f1}$ |
|---|---|---|---|
| 8.0 μH | 60.0 μH | 19.0 μH | 23.8 μH |
| $L_{f2}$ | $C_P$ | $C_S$ | $C_{f1}$ |
| 5.3 μH | 53.0 nF | 178.0 nF | 130.0 nF |
| $C_{f2}$ | $U_L$ | $I_{Lref}$ | $U_{dc}$ |
| 532.0 nF | 48 V | 30 A | 400 V |
| $N_P$ | $N_S$ | $N_{f2}$ | $f$ |
| 6 | 6 | 4 | 100 kHz |

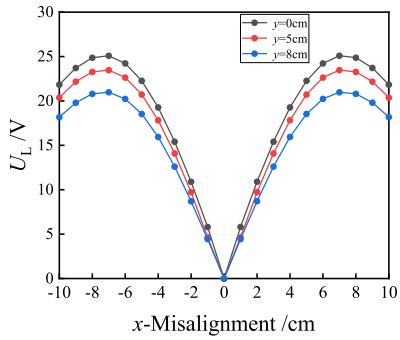


Fig. 10. Relationship between $U_L$ and $x$-misalignment under three different $y$-misalignment conditions ($y = 0$, 5, and 8 cm).

compensating capacitors can be determined. The parameters of the system are listed in Table I, where $N_p$, $N_{f2}$, and $N_S$ are 6, 4, and 6, respectively. The diameters of $L_{f1}$ and $L_P$ are 3.4 mm, while the diameters of $L_{f2}$ and $L_S$ are 6.5 mm.

### A. Self-Alignment Based on the Magnetic Coupling Structure

Fig. 10 illustrates the relationship between the $x$-misalignment and the output voltage $U_L$ in the self-alignment stage. It can be seen that $U_L$ fluctuates with $x$, and this article utilizes such fluctuation for self-alignment. The AGV is well-aligned and ready to be charged when the $x$-misalignment tends to 0. Due to the symmetrical coupling structure, this article only tests the positive direction of the $y$-axis. Under three different $y$-misalignment

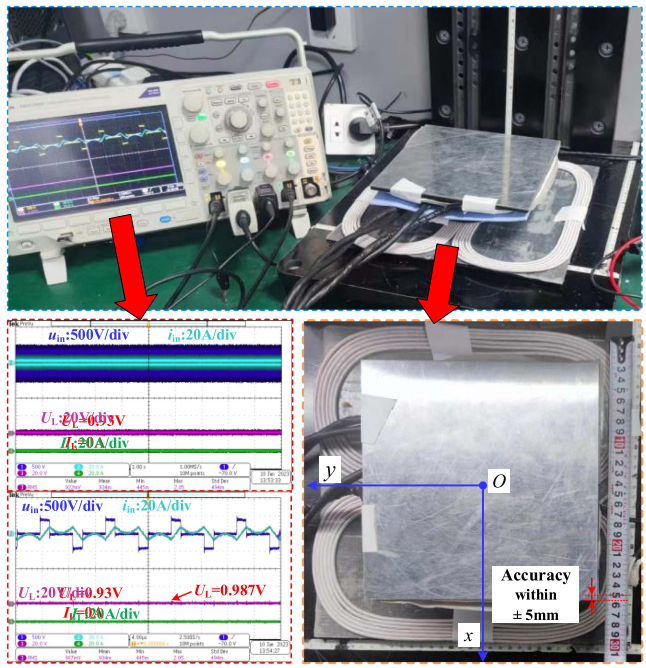


Fig. 11. Measured alignment accuracy of the proposed method.

conditions ($y = 0$, 5, and 8 cm), $U_L$ constantly tends to 0 when there is no $x$-misalignment. This shows that the self-alignment is not affected by the $y$-misalignment and is only associated with $x$-misalignment, which agrees with the theoretical analysis of the magnetic coupling structure.

In the experiment, the error index $\alpha$ is set as 1 V, and the designed magnetic coupler can achieve alignment accuracy within $\pm$ 5 mm, as shown in Fig. 11, i.e., during the self-alignment process, the measured $U_L$ is 0.987 V, and the receiver side is considered to be well-aligned.

### B. Dynamic Response From Self-Alignment Stage to Normal Charging Stage

Fig. 12 demonstrates the dynamic response from the self-alignment stage to the normal charging stage by circuit reconfiguration. Before the switching, the system works in the *LCC*-S topology for the purpose of the self-alignment. After the alignment process, the system enters the *LCC–LCC* topology (i.e., the normal charging stage). In the early stage of normal charging, there is a soft start process to ensure a safe system operation [16]. As can be seen from Fig. 12, the output current $i_{\rm in}$ of the inverter lags slightly behind the output voltage $u_{\rm in}$ of the inverter, indicating that the impedance of the inverter is inductive. The small phase angle of $i_{\rm in}$ lagging $u_{\rm in}$ ensures zero-voltage switching of the full-bridge switches and can eliminate the most reactive power [17].

Fig. 13(a) and (b) indicates the voltage and current stresses of switch $S$ in *LCC*-S configuration and *LCC–LCC* configuration, respectively. As shown in Fig. 13, $u_{\rm sw}$ and $i_{\rm sw}(i_S)$ represent the voltage of switch $S$ and the current flowing through $S$, respectively. Fig. 13(a) indicates that in the *LCC*-S configuration, the peak voltage of $u_{\rm sw}$ is around 70 V, and there is almost no current

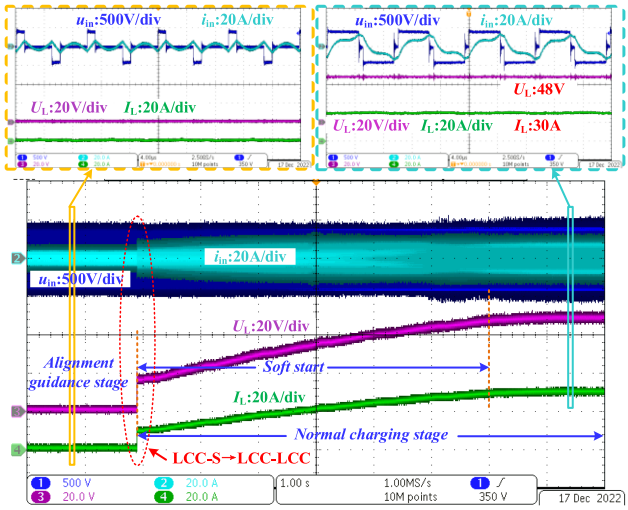


Fig. 12. Dynamic response from the *LCC*-S topology to the *LCC–LCC* topology.

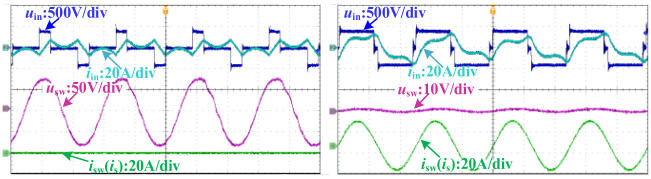


Fig. 13. Voltage and current stresses of switch $S$ in (a) *LCC*-S configuration and (b) *LCC–LCC* configuration.

flowing through switch $S$ due to the open-circuit condition. Fig. 13(b) indicates that in *LCC–LCC* configuration, the peak current of $i_{\mathrm{sw}}$ is around 24 A, and the peak voltage of $u_{\mathrm{sw}}$ is approximately 1 V. The voltage and current stresses of MOSFET $S_1$ and $S_2$ are within their current and voltage capacities.

### C. Dynamic Response With Load Change

Fig. 14 shows the dynamic response of the system when the load varies. First, the load is changed from 1.6 to 1.2 Ω. The voltage $U_L$ varies from 48 to 36 V. The current $I_L$ is controlled to 30 A. The corresponding dynamic response is 600 ms, and the overshoot of the current is 35 A. Second, the load is changed from 1.2 to 1.6 Ω. The current $I_L$ is then controlled to 30 A. The voltage $U_L$ varies from 36 to 48 V. The corresponding dynamic response is 500 ms and the undershoot of the current is 28 A.

### D. Interference Rejection

Fig. 15 shows the dynamic response of the system when $y$ varies. First, $y$ is changed from 0 to 8 cm. The mutual inductance is accordingly changed from 8 to 6.6 $\mu$H. Current $I_L$ and voltage $U_L$ are then controlled to 30 A and 48 V, respectively. The corresponding dynamic response is 300 ms and the undershoot of the current is 27 A. Second, $y$ is changed from 8 to 0 cm. The mutual inductance is accordingly changed from 6.6 to 8 $\mu$H. Current $I_L$ and voltage $U_L$ are then controlled to 30 A and 48 V, respectively. The corresponding dynamic response is 400 ms and the overshoot of the current is 34 A.

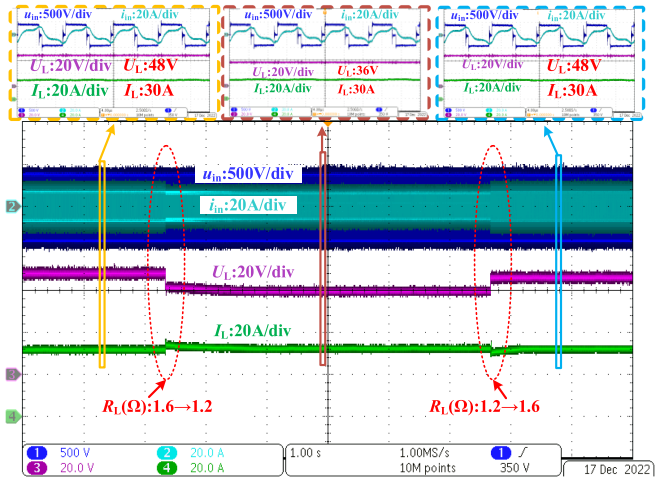


Fig. 14. Dynamic response when the load varies from 1.6 to 1.2 Ω and back to 1.6 Ω again.

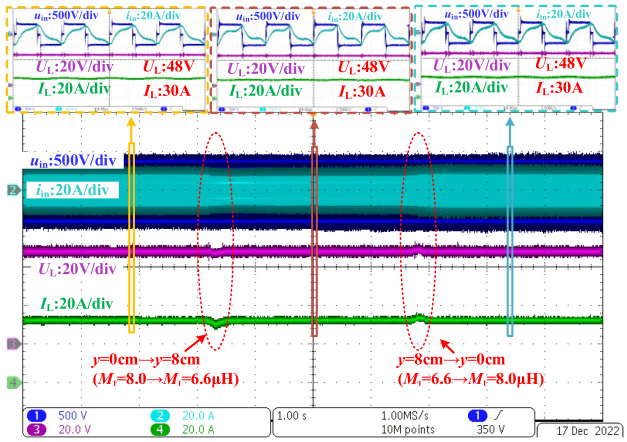


Fig. 15. Dynamic response of the interference rejection process ($y$ varies from 0 to 8 cm and back to 0 cm again).

### E. Output Current Control

Fig. 16 illustrates the dynamic response when $I_{L\mathrm{ref}}$ changes. As shown in Fig. 7, the current can be regulated by adjusting reference $I_{L\mathrm{ref}}$ by the primary-side controller to realize variable output current values. Fig. 16 depicts that the reference current $I_{L\mathrm{ref}}$ is set from 30 to 24 A and back to 30 A again, and the output current $I_L$ can be controlled to the target value accordingly.

The power efficiencies obtained from experiments under different $x$ misalignments are shown in Fig. 17, where $R_L = 1.6\ \Omega$. As can be seen from Fig. 17, the well-aligned system has the highest efficiency (89.1%) compared with the misaligned situations. A higher misalignment leads to lower power efficiency. Fig. 18 shows the measured power loss distribution under the rated output power condition of the well-aligned system, where the total power loss is 176.16 W, and the loss of switch $S$ is 10.76 W.

TABLE II
COMPARISON BETWEEN THIS ARTICLE AND ARTICLES PRESENTED IN [4], [5], [6], [7], [8], [9], [12], [13], AND [18]

| Reference | Method | Cost | Accuracy(mm) | Level | Characteristic |
|---|---|---|---|---|---|
| [4] | Camera | High | 22 | Easy | Add auxiliary camera |
| [5] | Ultrasonic sensors | High | -- | Easy | Increase the ultrasonic device |
| [6] | RFID | High | -- | Easy | Add RFID modules |
| [7] | Mutual inductance detection | Low | 1(simulated) | Hard | Detect the mutual inductance with a complicated algorithm |
| [8] | Primary AC current, maximum current detection | Low | -- | Hard | Detect the maximum primary AC current |
| [9] | Secondary AC current, sudden change detection | Low | -- | Hard | Detect the sudden change of the secondary AC current |
| [12] | By adding auxiliary minor coils, the lookup table method | High | 20 | Normal | Add four auxiliary coils and the related sensing circuits; Determine the desired position by the lookup table |
| [13] | By adding sensing coils, the fingerprint map comparison method | High | 15 | Normal | Add three differential connection sensing coils and the related sensing circuits; By matching the measured received signal strength (RSS) with the fingerprint map to obtain the offset coordinates |
| [18] | Intrinsic attractive force, mechanical structure | High | -- | Normal | Use the intrinsic attractive force with the mechanical structure to facilitate the auto-alignment |
| This article | Secondary DC voltage, tending to 0 | Low | ±5 | Easy | No additional components; Use DC sample and detection |

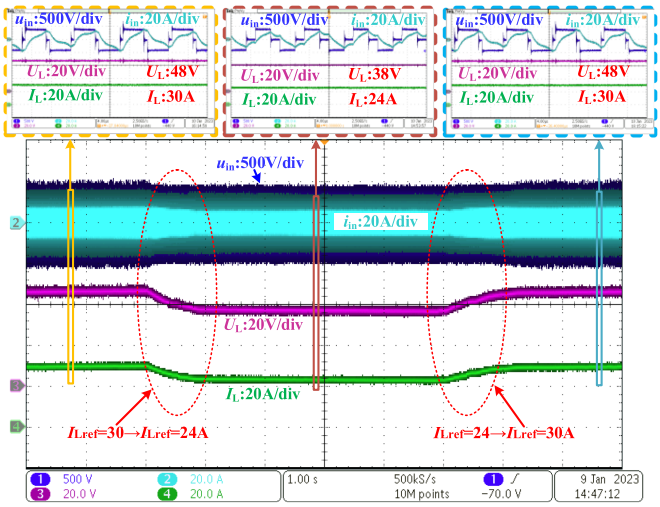


Fig. 16. Dynamic response when $I_{Lref}$ changes from 30 to 24 A and back to 30 A again.

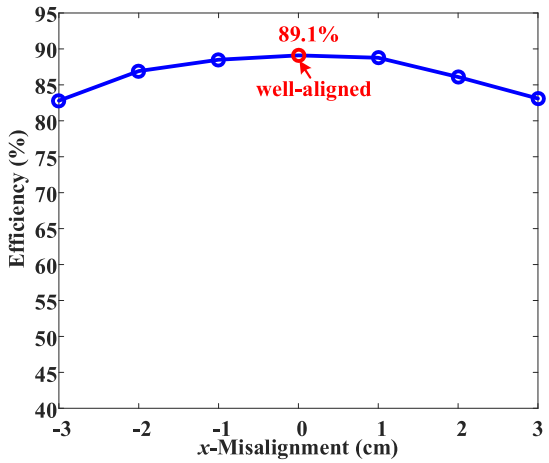


Fig. 17. Experimental efficiencies with different $x$ misalignments.

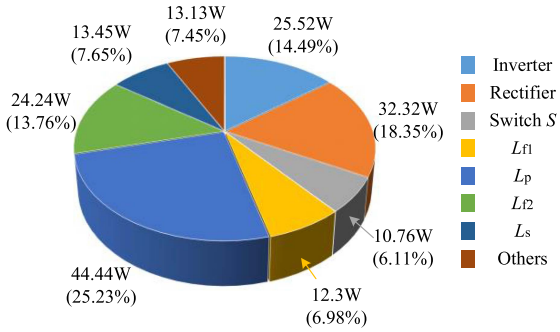


Fig. 18. Measured power loss distribution.

## V. DISCUSSION

### A. Advantages of the Proposed Self-Alignment Method

A comparison between this article and articles presented in [4], [5], [6], [7], [8], [9], [12], [13], and [18] is summarized in Table II. Compared to [4], [5], and [6], the proposed system avoids using costly auxiliary equipment, such as cameras and sensors. Compared to [7], [8], and [9], the proposed method is more straightforward and easier to implement by sampling dc voltages. Compared to [12] and [13], this article utilizes a configurable coil and circuit structure to support the self-alignment. Apart from the passive components used for WPT, no additional components, such as dedicated sensing coils and sensing circuits (i.e., four auxiliary coils and the related sensing circuits in [12]; three differential connection sensing coils and the related sensing circuits in [13]), are needed. Compared to [18], the proposed method is more straightforward and can realize the self-alignment without using the additional mechanical structure.

### B. Key Contributions of This Work

Although the coil structure, the compensation topology switching, and the control method used in this article look similar

TABLE III
COMPARISON BETWEEN THIS ARTICLE AND ARTICLES PRESENTED IN[19], [20], AND [21]

| Reference | Coil structure | Compensation Topology Switching | Control Method | Objective |
|---|---|---|---|---|
| [19] | Planar coil | SS→S-LCC | $S_1$ OFF, $S_2$ ON→$S_1$ OFN, $S_2$ OFF | CC and CVswitching |
| [20] | Planar square coil | Full-bridge-rectifier mode→ Double-voltage- rectifier mode | $Q_5$ OFF→$Q_5$ ON | Improve misalignment tolerance |
| [21] | Not mentioned | SS→LCC–LCC | $S_1$, $S_2$ OFF→$S_1$, $S_2$ ON | Improve system efficiency |
| This article | DD-coil and Q-coil | LCC-S→LCC–LCC | S OFF→S ON | Self-alignment |

TABLE IV
COMPARISON BETWEEN THIS ARTICLE AND ARTICLES PRESENTED IN [2], [3], [22], [23], AND [24]

| Ref | Efficiency | Output power |
|---|---|---|
| [2] | 90.93% | 500 W |
| [3] | 84.5% | 58.9 W |
| [22] | 86.1 % | 1.78 kW |
| [23] | 89.9% | 1.8 kW |
| [24] | 80% | 100 W |
| This article | 89.1% | 1.44 kW |

to other studies, the main contributions are different. Table III presents a comparison between this article and articles presented in [19], [20], and [21], which shows that the coil structure, the compensation topology switching, and the control method are different, leading to different contributions. Mai et al. [19] present a hybrid topology with two ac switches to achieve the required CC or constant voltage (CV) charging. Sun et al. [20] propose a mode-switching-based method, which can significantly improve the misalignment tolerance of the WPT system by using the different driving modes of the rectifier. Rezazade et al. [21] focus on increasing WPT systems' efficiency through the proposed new hybrid topology that combines the SS and double-sided *LCC* topologies. The main contribution of this article is around the novel magnetic coupler design and control method to support the self-alignment of AGV and its wireless charging. Moreover, the self-alignment ensures good magnetic coupling before charging, contributing to a high mutual inductance and a high PTE.

### C. Comparison Results in Terms of Output Power and Efficiency

In terms of output power and efficiency of the AGV wireless charging system, the comparison results between this article and articles presented in [2], [3], [22], [23], and [24] are summarized in Table IV. As can be seen from Table IV, the output power of this article is close to that of [22] and [23], but higher than that of [2], [3], and [24]. The efficiency of this article is close to that of [2] and [23], but higher than that of [3], [22], and [24].

## VI. CONCLUSION

This article proposes a robust wireless charging system with self-alignment capability and controllable output current for AGVs. A Q-coil in the reconfigurable coupling structure is used to adjust the AGV position for self-alignment and as a compensation inductor for WPT. The self-alignment ensures that the coils are well-aligned before charging, which leads to a high PTE. A laboratory prototype with controllable output charging current is constructed, and the results show that the proposed system can realize an 89.1% dc–dc PTE at an output current of 30 A and a voltage of 48 V.

## REFERENCES

[1] J. S. Choi, S. Y. Jeong, B. G. Choi, S.-T. Ryu, C. T. Rim, and Y.-S. Kim, "Air-gap-insensitive IPT pad with ferromagnetic and conductive plates," *IEEE Trans. Power Electron.*, vol. 35, no. 8, pp. 7863–7872, Aug. 2020.
[2] C. Zhu et al., "Analysis and design of cost-effective WPT systems with dual independently regulatable outputs for automatic guided vehicles," *IEEE Trans. Power Electron.*, vol. 36, no. 6, pp. 6183–6187, Jun. 2021.
[3] H. Wang and K. W. E. Cheng, "A dual-receiver inductive charging system for automated guided vehicles," *IEEE Trans. Magn.*, vol. 58, no. 8, Aug. 2022, Art. no. 8700905.
[4] N. Isozaki, D. Chugo, S. Yokota, and K. Takase, "Camera-based AGV navigation system for indoor environment with occlusion condition," in *Proc. IEEE Int. Conf. Mechatron. Autom.*, 2011, pp. 778–783.
[5] Y. Sakayanagi, S. Togawa, K. Konagaya, and Y. Kuwahara, "Wireless power transmission for a traveling mobility scooter," in *Proc. IEEE Wireless Power Transfer Conf.*, 2016, pp. 1–3.
[6] S. Chen, C. Liao, and L. Wang, "Research on positioning technique of wireless power transfer system for electric vehicles," in *Proc. IEEE Conf. Expo. Transp. Electrific. Asia-Pacific*, 2014, pp. 1–4.
[7] Y. Zou and S. O'Driscoll, "Implant positioning system using mutual inductance," in *Proc. IEEE Annu. Int. Conf. Eng. Med. Biol. Soc.*, 2012, pp. 751–754.
[8] X. Li, J. Hu, H. Wang, X. Dai, and Y. Sun, "A new coupling structure and position detection method for segmented control dynamic wireless power transfer systems," *IEEE Trans. Power Electron.*, vol. 35, no. 7, pp. 6741–6745, Jul. 2020.
[9] J. Sithinamsuwan, H. Fujimoto, and Y. Hori, "Sensorless vehicle position detection in electric vehicle by logistic estimation function of mutual inductance," in *Proc. IEEE PELS Workshop Emerg. Technol., Wireless Power Transf.*, 2020, pp. 254–259.
[10] D. Kobayashi, T. Imura, and Y. Hori, "Real-time coupling coefficient estimation and maximum efficiency control on dynamic wireless power transfer for electric vehicles," in *Proc. IEEE PELS Workshop Emerg. Technol., Wireless Power*, 2015, pp. 1–6.
[11] X. Dai, X. Li, Y. Li, and A. P. Hu, "Maximum efficiency tracking for wireless power transfer systems with dynamic coupling coefficient estimation," *IEEE Trans. Power Electron.*, vol. 33, no. 6, pp. 5005–5015, Jun. 2018.
[12] Y. Gao, C. Duan, A. A. Oliveira, A. Ginart, K. B. Farley, and Z. T. H. Tse, "3-D coil positioning based on magnetic sensing for wireless EV charging," *IEEE Trans. Transp. Electrific.*, vol. 3, no. 3, pp. 578–588, Sep. 2017.
[13] B. Zhang et al., "Triple-coil-structure-based coil positioning system for wireless EV charger," *IEEE Trans. Power Electron.*, vol. 36, no. 12, pp. 13515–13525, Dec. 2021.
[14] H. Wang and K. W. E. Cheng, "Analysis, design, and validation of a decoupled double-receiver wireless power transfer system with constant voltage outputs for industrial power supplies," *IEEE Trans. Ind. Inform.*, vol. 19, no. 1, pp. 362–370, Jan. 2023.

[15] M. Budhia, J. T. Boys, G. A. Covic, and C.-Y. Huang, "Development of a single-sided flux magnetic coupler for electric vehicle IPT charging systems," *IEEE Trans. Ind. Electron.*, vol. 60, no. 1, pp. 318–328, Jan. 2013.
[16] L. Wang et al., "Mutual inductance identification of IPT system based on soft-start process," *IEEE Trans. Power Electron.*, vol. 37, no. 6, pp. 7504–7517, Jun. 2022.
[17] X. Qu, H. Han, S.-C. Wong, C. K. Tse, and W. Chen, "Hybrid IPT topologies with constant current or constant voltage output for battery charging applications," *IEEE Trans. Power Electron.*, vol. 30, no. 11, pp. 6329–6337, Nov. 2015.
[18] A. Namadmalan, R. Tavakoli, S. M. Goetz, and Z. Pantic, "Self-aligning capability of IPT pads for high-power wireless EV charging stations," *IEEE Trans. Ind. Appl.*, vol. 58, no. 5, pp. 5593–5601, Sep./Oct. 2022.
[19] R. Mai, Y. Chen, Y. Li, Y. Zhang, G. Cao, and Z. He, "Inductive power transfer for massive electric bicycles charging based on hybrid topology switching with a single inverter," *IEEE Trans. Power Electron.*, vol. 32, no. 8, pp. 5897–5906, Aug. 2017.
[20] J. Sun, Y. Wang, Z. Sun, and D. Xu, "A mode-switching-based method to improve misalignment tolerance of WPT systems," in *Proc. IEEE 25th Int. Conf. Elect. Mach. Syst.*, 2022, pp. 1–5.
[21] S. Rezazade, A. Shahirinia, R. Naghash, N. Rasekh, and S. E. Afjei, "A novel efficient hybrid compensation topology for wireless power transfer," *IEEE Trans. Ind. Electron.*, vol. 70, no. 3, pp. 2277–2285, Mar. 2023.
[22] F. Lu et al., "A tightly coupled inductive power transfer system for low-voltage and high-current charging of automatic guided vehicles," *IEEE Trans. Ind. Electron.*, vol. 66, no. 9, pp. 6867–6875, Sep. 2019.
[23] F. Lu et al., "A low-voltage and high-current inductive power transfer system with low harmonics for automatic guided vehicles," *IEEE Trans. Veh. Technol.*, vol. 68, no. 4, pp. 3351–3360, Apr. 2019.
[24] H. Matsumoto, Y. Shibako, and Y. Neba, "Contactless power transfer system for AGVs," *IEEE Trans. Ind. Electron.*, vol. 65, no. 1, pp. 251–260, Jan. 2018.

**Xiaofei Li** (Member, IEEE) received the B.E. degree in automation, and the Ph.D. degree in control theory and control engineering from Chongqing University, Chongqing, China, in 2013, and 2018, respectively.

From 2018 to 2019, he was a Research Associate with the Department of Electrical Engineering, The Hong Kong Polytechnic University. He is currently an Associate Professor with Chongqing University, Chongqing, China. His research interests include modeling and control of wireless power transfer and power electronics.

**Cheng Wang** received the M.Sc. degree in transportation information engineering and control from Chongqing University, Chongqing, China, in 2023, where he is currently working toward the Ph.D. degree in control theory and control engineering.

His main research interest is wireless power transfer.

**Heshou Wang** received the M.Sc. and Ph.D. degrees in electrical engineering from The Hong Kong Polytechnic University, Hong Kong, in 2018 and 2022, respectively.

From 2018 to 2019, he was a Research Assistant with the Department of Electrical Engineering, The Hong Kong Polytechnic University, where he is currently a Postdoctoral Fellow. His main research interests include applied electromagnetics, wireless power transfer, and electric vehicles.

**Xin Dai** (Member, IEEE) received the B.E. degree in industrial automation from Yuzhou University, Chongqing, China, in 2000, and the Ph.D. degree in control theory and control engineering from the College of Automation, Chongqing University, Chongqing, China, in 2006.

In 2012, he was a Visiting Scholar with The University of Auckland, Auckland, New Zealand. He is currently a Professor with the College of Automation, Chongqing University. His current research interests include inductive power transfer technology and nonlinear dynamic behavior analysis of power electronics.

**Yue Sun** (Member, IEEE) received the B.E. degree in electrical engineering, the M.E. degree in industrial automation, and the Ph.D. degree in mechanical and electrical integrated manufacturing from Chongqing University, Chongqing, China, in 1982, 1988, and 1995, respectively.

In 1997, he was a Senior Visiting Scholar with the University of Valenciennes, France. He is currently a Professor with the School of Automation, Chongqing University. His current research interests include automatic control, wireless power transfer, and power electronics' applications.

**Aiguo Patrick Hu** (Senior Member, IEEE) received the B.E. and M.E. degrees in electrical engineering from Xi'an Jiaotong University, Xi'an, China, in 1985 and 1988, respectively, and the Ph.D. degree in electrical and electronic engineering from The University of Auckland, Auckland, New Zealand, in 2001.

He stayed with the National University of Singapore, Singapore, for a semester as an exchange Postdoctoral Research Fellow. He has authored more than 200 peer-reviewed journal and conference articles with about 4500 citations, authored the first monograph on inductive power transfer technology, and contributed four book chapters on wireless power transfer modeling and control, as well as electrical machines. He is currently a Full Professor with the Department of Electrical and Electronic Engineering, University of Auckland. His research interests include wireless/contactless power transfer systems and application of power electronics in renewable energy systems.

Dr. Hu was a recipient of the University of Auckland VC's Funded Research and Commercialization Medal in April 2017.